Heliyon 10 (2024) e30743

Contents lists available at ScienceDirect

Heliyon

journal homepage: www.cell.com/heliyon

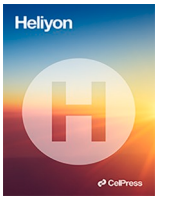

Research article

Formulation optimization of lyophilized aptamer-gold nanoparticles: Maintained colloidal stability and cellular uptake

Dalya Saidi [a,1], Marya Obeidat [a,*,1], Shrouq Alsotari [b], Abed-Alqader Ibrahim [c], Rula Al-Buqain [b], Suha Wehaibi [b], Dana A. Alqudah [b], Hamdi Nsairat [d], Walhan Alshaer [b], Alaaldin M. Alkilany [e,**]

[a] *Department of Medical Laboratory Sciences, Faculty of Applied Medical Sciences, Jordan University of Science and Technology, Irbid, 22110, Jordan*
[b] *Cell Therapy Center, The University of Jordan, Amman, 11942, Jordan*
[c] *Department of Nanoscience, Joint School of Nanoscience and Nanoengineering, University of North Carolina at Greensboro, 2907 E. Gate City Blvd, Greensboro, NC, 27401, USA*
[d] *Pharmacological and Diagnostic Research Center, Faculty of Pharmacy, Al-Ahliyya Amman University, Amman, 19328, Jordan*
[e] *College of Pharmacy, QU Health, Qatar University, Doha, 2713, Qatar*

A R T I C L E I N F O

Keywords:
Aptamer
Gold nanoparticles
Aggregation
Cryoprotectants
Lyophilization

A B S T R A C T

Anti-nucleolin (NCL) aptamer AS1411 is the first anticancer aptamer tested in clinical trials. Gold nanoparticles (AuNP) have been widely exploited for various biomedical applications due to their unique functional properties. In this study, we evaluated the colloidal stability and targeting capacity of AS1411-funtionalized AuNP (AuNP/NCL-Apt) against MCF-7 breast cancer cell line before and after lyophilization. Trehalose, mannitol, and sucrose at various concentrations were evaluated to determine their cryoprotection effects. Our results indicate that sucrose at 10 % (w/v) exhibits the best cryoprotection effect and minimal AuNP/NCL-Apt aggregation as confirmed by UV–Vis spectroscopy and dynamic light scattering (DLS) measurements. Moreover, the lyophilized AuNP/NCL-Apt at optimized formulation maintained its targeting and cytotoxic functionality against MCF-7 cells as proven by the cellular uptake assays utilizing flow cytometry and confocal laser scanning microscopy (CLSM). Quantitative PCR (qPCR) analysis of nucleolin-target gene expression also confirmed the effectiveness of AuNP/NCL-Apt. This study highlights the importance of selecting the proper type and concentration of cryoprotectant in the typical nanoparticle lyophilization process and contributes to our understanding of the physical and biological properties of functionalized nanoparticles upon lyophilization.

1. Introduction

Despite continuous advances in the current treatments and diagnostic/imaging tools for different diseases, there is still an urgent

* Corresponding author. Department of Medical Laboratory Sciences, Faculty of Applied Medical Sciences, Jordan University of Science and Technology, Irbid, 22110, Jordan.
** Corresponding author. College of Pharmacy, Qatar University, Doha, 2713, Qatar.
E-mail addresses: mmobeidat82@just.edu.jo (M. Obeidat), alkilany@qu.edu.qa (A.M. Alkilany).
[1] Contributes equally.

https://doi.org/10.1016/j.heliyon.2024.e30743
Received 9 January 2024; Received in revised form 1 May 2024; Accepted 3 May 2024
Available online 8 May 2024

need for new, precise, and safe therapeutic and diagnostic/imaging options. The concept of a "magic bullet" still inspires researchers to develop targeted drug delivery systems that save normal cells and reach diseased ones [1]. The unmet needs of any disease treatment do fit this paradigm, emphasizing the importance of developing targeted drug delivery systems. Nanotechnology has enabled targeted delivery of different drugs to cancer cells, which has led to a significant reduction in their systemic side effects [2]. Several types of nanomedicines have been reported to date, with promising potential to treat various diseases, especially cancer [3]. Most nanomedicines lack specificity towards their target cells. A promising approach in this field consists of designing multifunctional drug nanocarriers that are functionalized with targeting ligands that support targeting and stimuli-responsive drug release in a selective manner [4]. Several types of targeting ligands can be used to guide nanocarriers to tumor cells, including small molecules, proteins, peptides, sugars, antibodies, and aptamers [5,6].

Aptamers (from the Latin word "aptus", meaning fit, and the Greek word "meros", meaning part or unit) are short, single-stranded DNA (ssDNA) or RNA oligonucleotides with the capability to fold into unique and complex three-dimensional structures [7]. Aptamers can bind to an unlimited variety of targets, like small molecules, ions, protein targets, or even whole living cells, with high affinity and specificity [8,9]. Aptamers possess many appealing features that make them promising targeting moieties. For example, compared with bulky antibodies, aptamers have a smaller size and a flexible structure, allowing them to bind to smaller targets or hidden domains that are inaccessible to larger antibodies. Morover, aptamers can be selected against a wide range of targets, including toxic and non-immunogenic molecules that antibodies cannot recognize [10].

Anti-nucleolin aptamer AS1411 is a G-quadruplex (G4) that has proven clinical activity, along with various examples of disease stabilization and many cases of long-lasting objective reactions [11,12]. AS1411 aptamer can be conjugated to various nanomaterials and is considered the first anticancer aptamer tested in clinical trials [13–15]. Conjugation of AS1411 aptamer to gold nanospheres increases its accumulation inside cancer cells and enhances its antitumor activity *in vivo* [16,17]. Moreover, AS1411 aptamer-functionalized nanoparticles exhibit an enhanced cellular targeting efficiency against different cancers compared to non-targeting nanoparticles due to the high affinity of AS1411 aptamer toward the overexpressed nucleolin receptor in cancer cells [13,18,19]. However, in phase I and phase II clinical trials, AS1411 aptamer exhibited low therapeutic potency due to its rapid clearance from the body [20]. Therefore, functionalizing different nanoparticles with AS1411 aptamer has been successfully performed and showed higher selectivity and accumulation in tumor cells, improving cytotoxicity and antiproliferative effects [3].

Gold nanoparticles (AuNP) are inorganic NPs widely employed in nanomedicine applications in therapy, imaging, detection, diagnostics, and precise drug delivery [21–28]. AuNP have a unique particle-light interaction owing to the surface plasmon resonance (SPR) effect and multiple surface functionalities [29,30]. AuNP can be used alone or functionalized with several targeting ligands, such asoligonucleotides, antibodies, and proteins, making them promising candidates for designing novel targeting bio-nanomaterials for a wide range of biomedical applications [31,32]. Several reports described the successful functionalization of AuNP with AS1411 aptamer to enhance potency, imaging specificity, and sensitivity [33–45].

Although functionalizing nanoparticles with aptamers enhances the targeting capacity and therapeutic/diagnostic potency, the poor colloidal stability of functionalized nanoparticles in aqueous suspensions is one challenge that limits the bench-to-bedside translation [6,46,47]. Lyophilization of nanoparticle formulations is a common process to increase colloidal stability and shelf life used in academic reserach and industrial settings. A recent relevant example is the challenge in the transportation and storage of the COVID vaccine, which is an mRNA complexed with lipid nanoparticles. The mRNA component of the vaccine and the stability of the lipid nanoparticles pose significant difficulties due to the intrinsic instability of the mRNA as well as the colloidal stability and protective capability of the lipid nanoparticles used as carriers. The attributes related to the colloidal stability of the lipid nanoparticles explain why the Pfizer-BioNTech vaccine requires storage temperatures as low as −80 to −60 °C, while the Moderna vaccine can be stored at −25 to −15 °C. It is worth noting that significant ongoing efforts are focused on developing a lyophilized version of these vaccines to enhance the overall stability of the mRNA-nanoparticle formulations. However, the lyophilization process may generate stresses against nanoparticles; therefore, cryoprotectants such as sucrose, maltose, lactose, and trehalose are needed to prevent nanoparticles collapse/aggregation during the lyophilization process [48,49].

Based on the promising properties and applications of aptamers and AuNP in therapy and diagnosis, this study aimed to synthesize gold nanospheres functionalized with AS1411 aptamer (AuNP/NCL-Apt) and investigate their colloidal stability upon lyophilization (freeze-drying) process in the presence of various commonly used cryoprotectants. Moreover, lyophilized AuNP/NCL-Apt were further evaluated for their targeting capacity against MCF-7 breast cancer cell line.

2. Materials and methods

2.1. Materials

Gold-III chloridetri-hydrate (HAuCl4), mannitol, sucrose, trehalose, phosphate buffer saline (PBS), tris(2-carboxyethyl) phosphine (TCEP), and trypsin inhibitor were obtained from Sigma-Aldrich and used as received. Trisodiumcitrate (TSC) was purchased from HiMedia. All the stock solutions and dilutions were prepared using Milli-Qwater. Nucleolin-thiolated aptamer AS1411 (positive sequence) (5′-GGTGGTGGTGGTTGTGGTGGTGGTGGT TTTTTT TTT TTT -3′) (thiol C6 SS), Alexa flour 647-tagged AS1411 (positive sequence) (5′- Alexa 648- GGT GGT GGT GGT TGT GGT GGT GGTGGT TTT TTT TTT TTT -346-S-S-C6-3′), Bcl-2 primers, forward:5′-GATGGGATCGTTGCCTTATGC-3′ and reverse:5′-GTCTACTTCCTCTGTGATGTTGT -3′, and Beta-actin control primers, forward:5′-ACAGAGCCTCGCCTTTGCC -3′ and reverse:5′-GATATCATCATCCATGGTGAGCTGG -3′, were purchased from Integrated DNA Technologies (IDT) Inc (Coralville, IA, USA). 6-Diamidino-2-phenylindole dihydrochloride (DAPI) was fromMerck Millipore (USA) and Ethidium bromide was from Fisher Scientific Ltd (England). Accutase and fetal bovine serum (FBS) were purchased from Capricorn

Scientific GmbH (Germany). Glomax microplate reader and QuantiFluor® ssDNA Kit were from Promega (USA). Mini-RNeasy kit was from Qiagen (USA). PrimeScript RT Master Mix (Cat No. RR036A) and SYBR Premix Ex *Taq*II (Tli RNaseH Plus) (Cat No. RR820L) were from Takara (China). PCR purification kit was purchased from Thermo Scientific Gene JET. All chemicals and solvents were of analytical grade. Aqua regia solution was freshly prepared by mixing hydrochloric acid (HCl) with nitric acid (HNO3) in a ratio of 3:1 v/v. All reagents and chemicals were used without further treatment.

2.2. Synthesis of citrate-capped AuNP (Cit-AuNP) (18 nm core diameter)

Spherical AuNP was synthesized using a modified protocol reported by Bastus et al. [50]. Briefly; 150 mL of a 1.32 mM sodium citrate solution (0.2 mmol, 8 equivalent) was transferred to a 250 mL three-necked round-bottom flask associated with a condenser and heated up until boiling under vigorous stirring. After 5 min of boiling, 1.5 mL of 25 mM tetra chloroauric acid ($HAuCl_4$, 0.025 mmol, 1 equivalent) was injected. A color change was immediately observed from pale yellow to light blue and then to ruby red. The solution was further boiled for 10 min to allow the AuNP to grow and then cooled down with stirring to room temperature.

2.3. UV/vis absorption spectroscopy

The optical properties of AuNP were evaluated by an ultraviolet–visible (UV–Vis) spectrophotometer. Absorption spectra for Cit-AuNP and AuNP/NCL-APT suspensions before and after freeze-drying were recorded over the range 400–800 nm using Spectrascan 80D (Biotech Eng., UK).

2.4. Dynamic light scattering (DLS) measurements

The average hydrodynamic diameter, poly dispersity index (PDI) and zeta potential of free AuNP and AuNP/NCL-Apt before and after freeze-drying were measured by DLS on a Zeta-sizer (Nano-ZS) (Malvern Instruments Ltd., Malvern, UK). AuNP and AuNP/NCL-Apt before and after freeze-drying were diluted with nuclease-free water. All samples were equilibrated at room temperature for 60 s before the DLS measurement [51].

2.5. Transmission electron Microscopy (TEM)

The size and shape of free AuNP and AuNP/NCL-APT were examined by transmission electron microscopy (TEM) using 200-mesh formvar copper grids (SPI supplies, USA). A drop of purified nanoparticle suspension (10 nM) was located on the copper grid followed by air-drying at room temperature overnight. The dried samples were visualized using Versa 3D TEM at a running voltage of 30 KV (FEI, Netherlands) [52].

2.6. AS1411 aptamer conjugation to AuNP

The final concentration of AuNP was set at 30 nM using formula C = A450/ε450(d), (C: concentration, A: absorbance at 450 for a standard path length of 1 cm, and ε450(d): data of ε450) [53]. AS1411 aptamer was first treated with 100 mM TCEP (PH 6.5) for 1 h at room temperature to break the disulfide bonds and produce AS144-SH [54], then it was conjugated to AuNP (average particle size = 18 nm) by gentle mixing (AuNP:aptamer is 1:50 M ratio). The final mixture was incubated overnight at room temperature under gentle stirring to facilitate the binding of the aptamer to the gold surface via a thiol-gold coordination bond. Then, the suspension was centrifuged for 20 min at 13,000 rcf at 25 °C for two times to remove the free unconjugated aptamer (supernatant). After two washing steps, the pelleted AuNP/NCL-Apt was resuspended in free nuclease water [55].

2.7. Aptamer folding

AS1411 aptamer folding was performed by heating aptamers at 85 °C for 5 min, followed by incubation at room temperature for 5 min and further incubation on ice for 5 min. These steps involve denaturing the single-stranded oligonucleotides to allow aptamers to be folded into a complex three-dimensional conformational shape specific for target cell binding [56].

2.8. Quantification of aptamer density on AuNP

QuantiFluor® ssDNA kit was used to estimate the number of aptamers conjugated to one AuNP. This method includes a fluorescent DNA-binding dye (492 nm Ex/528 nm Em) that allows sensitive quantitation of minor quantities of single-stranded DNA (ssDNA). Briefly, AuNP were mixed with NCL-APT at different molar ratios, followed by centrifugation to pellet the AuNP, quantify the free NCL-APT in the supernatant, and then calculate the bound NCL-APT. As the concentration of added AuNP is known, the number of NCL-APT on each AuNP can be calculated. A standard curve of 6.25–400 ng/well was constructed to quantify the conjugated AS1411 aptamer. The fluorescent intensity of AS1411 aptamer before and after conjugation to AuNP was measured using Glomax microplate reader [57].

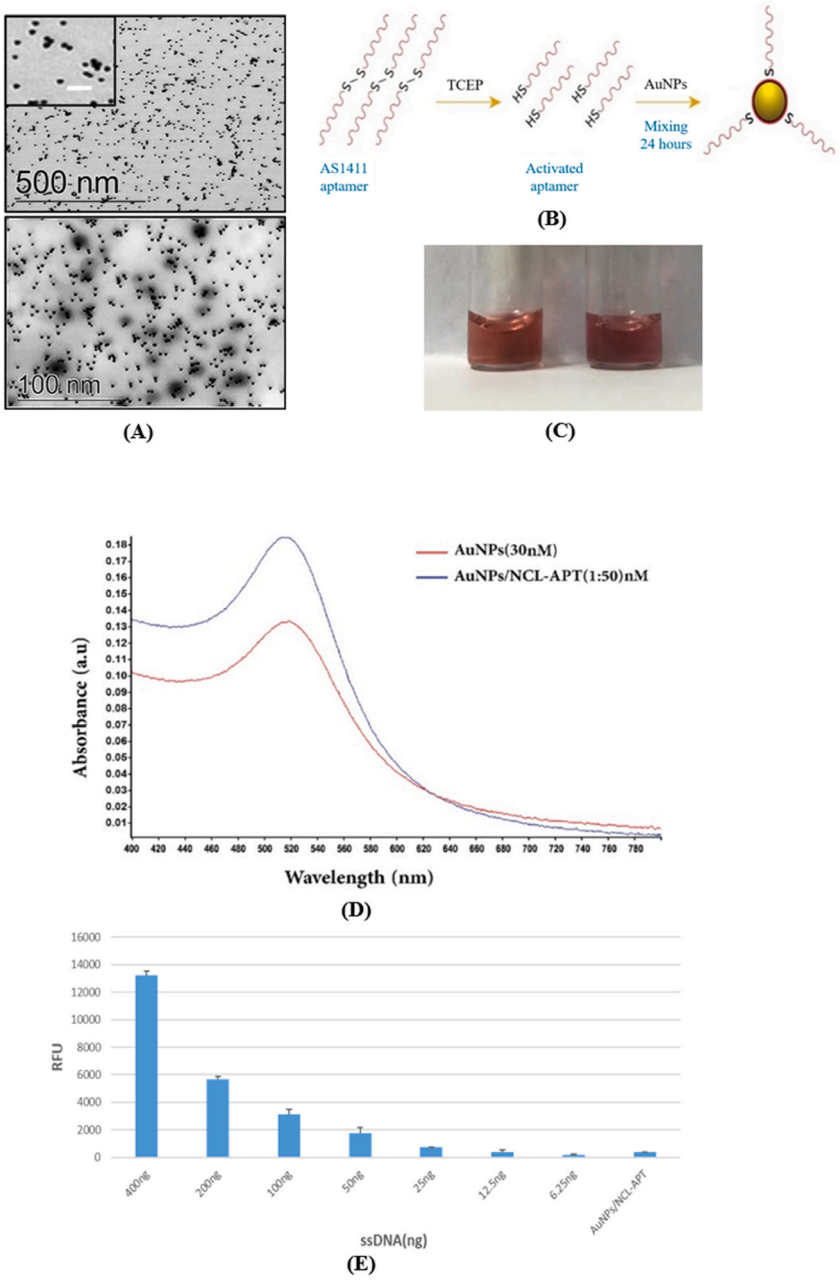

Fig. 1. Characteristics of AuNP and AuNP/NCL-APT preperations. (A) Representative TEM images of Citrate-capped AuNP (top). (Inset: Higher magnification with scale bar = 100 nm) and AuNP/NCL-APT **(**bottom**) (B)** A schematic view of AS1411 aptamer conjugation to a gold nanoparticle. **(C)** A representative photograph of AuNP suspension (left vial) and AuNP/NCL-APT suspension (right vial).**(D)** Absorption spectra of AuNP and AuNP/NCL-APT suspensions as labeled. **(E)** A ssDNA standard graph of the recommended standards (400, 200, 100, 50, 25, 12.5, 6.25 ng/well) and an AuNPs/NCL-APT sample. The values represent mean ± SD of 3 independent experiments. (For interpretation of the references to color in this figure legend, the reader is referred to the Web version of this article.)

2.9. Freeze-drying of AuNP/NCL-APT

The cryoprotectants mannitol, trehalose, and sucrose were dissolved in 200 μL of purified AuNP/NCL-Apt suspensions (30 nM in particles) at 2.5, 5, and 10 % (w/v) concentrations. The resultant suspensions were then frozen by fast immersion in liquid nitrogen for 5 min and then transferred directly to the freeze drier (HumanLab Instrument Co, Korea) using a reduced pressure ($<1 \times 10^{-3}$ bar) for 16 h. The freeze-dried samples were reconstituted in200 μL nuclease-free water for further evaluations [46].

Table 1
The Characterization of AuNP and AuNP/NCL-APT formulations. Values represent mean ± SD of 3 independent experiments.

Formulation	Particle size (Hydrodynamic diameter, nm)	Polydispersity index	Zeta potential (mV)	Maximum wavelength of the plasmon peak (nm)
AuNP	20.9+/-1.2	0.406+/-0.14	−26.8+/-4.2	517
AuNP/NCL-APT	55.4+/-1.7	0.48+/-0.16	−40.2+/-1.5	520

2.10. MCF7 cell culture

The MCF-7 human breast cancer cell line was obtained from the American Type Culture Collection (ATCC, Manassas, VA, USA). MCF-7 cells were cultured in RPMI 1640 medium supplemented with 10 % (v/v) fetal bovine serum (FBS), 100 U/mL penicillin, 100 mg/mL streptomycin, and 2 mM L-Glutamine, and maintained in a humidified 5 % CO_2 incubator (Memmert, Germany) at 37 °C. The cells were sub-cultivated approximately every 3 days, after reaching 90 % confluence, at a ratio of 1:5 using 0.05 % (w/v) trypsin-EDTA.

2.11. Flow cytometry of cellular uptake and aptamer density

MCF-7 cells were cultured at 5×10^5 seeding density in 6-well plates for 24 h to reach 70–80 % confluency before treatment. MCF-7 cells were treated with AuNP/Alexa-NCL-APT suspensions (30 nM in particles) for 4 h in a humidified 5 % CO_2 incubator at 37 °C. Cells were then washed three times with PBS, harvested using trypsin-EDTA, and transferred into 5 mL flow tubes for flow cytometry analysis. Around 10,000 events were counted using FACS Canto II (BD, USA) and analyzed using BD FACSDiva™ software version 8.0 (BD, USA). Cells treated with free AuNPor free AS1411 aptamer were used as negative control [57,58].

2.12. Confocal laser scanning microscopy analysis (CLSM)

MCF-7 cells were cultured at 5×10^5 seeding density on glass coverslips in 6-well plates for 24 h to reach 70–80 % confluency before treatment. Then, they were incubated with AuNP/Alexa-NCL-Apt suspensions (40 nM NCL-Apt) for 4 h in a humidified 5 % CO_2 incubator at 37 °C.Next, cells were fixed in 4 % formaldehyde for 20 min at room temperature in the dark, washed three times with PBS, and stained with the nuclear stain DAPI diluted in PBS at 1: 1500 for 15 min at room temperature in the dark. Finally, the coverslips were mounted on glass slides usinga fluorescent mounting medium (Dako Omnis). Confocal images were obtained by LSM 780 (Zeiss, Germany) using Plan-Apochromat 63×/1.4 Oil DIC M27 object and lasers 405 nm, 514 nm, and 633 nm for excitation of DAPI and Alexa-Fluor 647, respectively. The ranges of the detector's emission signals were 410–525 nm for DAPI and 637–755 nm for Alexa-Fluor 647 [58]. Untreated cells were used as a negative control.

2.13. Quantitative real-time PCR (qRT-PCR)

For gene expression analysis, MCF- 7 cells at 5×10^5 seeding density were treated for 24 h with 50 μL AuNP/NCL-APT (1:50 M ratio) before and after freeze-drying. Total RNA was extracted from cells using a mini-RNeasy kit according to the manufacturer's instructions and quantified by Nanodrop (Thermofisher, USA). A total of 0.5 μg RNA was reverse transcribed to cDNA using Prime-Script RT Master Mix. The qRT-PCR reaction mix was prepared by adding 25 ng cDNA, 200 nM primers targeting bcl-2 or GAPDH genes, 7.2 μL free nuclease water, and 10 μL SYBR Premix Ex *Taq*II. The gene amplification was performed on CFX96C1000 Touch thermal cycler (BioRad, USA) with the following temperature setting:(i) 95°Cfor 3 min, (ii) 40cyclesof 95 °C for 5 s and 61 °C for 30 s. Each sample was examined in triplicate and a mean cycle threshold (CT) value was calculated for bcl-2 and GAPDH genes. Delta CT (ΔCT) was calculated by subtracting housekeeping gene (GAPDH) mean CT from bcl-2 gene mean CT for each sample. ΔΔCT was determined by subtracting average ΔCT of test sample from that of negative control sample. Finally, data were analyzed according to $2^{-\Delta\Delta CT}$ method using CFX Maestro™ Software-Bio-Rad [59]. Untreated and cells treated with free APT or AuNP were used as a negative control.

3. Results and discussion

3.1. AuNP/NCL-APT preparation and characterization

Citrate-capped AuNPs (Cit-AuNPs) were prepared using the wet chemistry method that utilizes citrate anions as reducing and capping agents. The resulting Cit-AuNP had a core diameter of 18 nm, as confirmed by TEM analysis (Fig. 1A (top)). The surface of these nanoparticles is covered with citrate anions that are physically adsorbed to the gold surface, as evident from the zeta potential measurements shown in Table 1. The thiol-modified NCL-APT was conjugated to AuNPs through a gold-sulfur (Au–S) coordination bond that displaces the weakly adsorbed citrate anion as sketched in Fig. 1B. The morphology of nanoparticles is of ultimate significance to detect possible fusion or aggregation, thus TEM was utilized to evaluate the size and morphological features of the conjugates. As shown in Fig. 1A (bottom), the AuNPs/NCL-APT formulation demonstrates a homogeneous population of well-defined

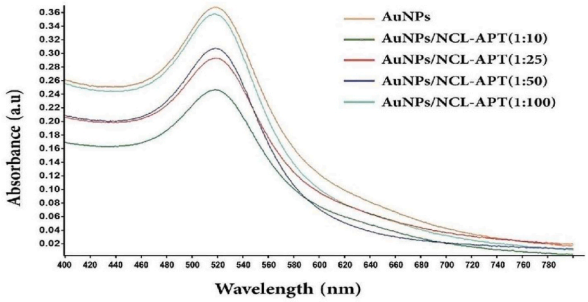

(A)

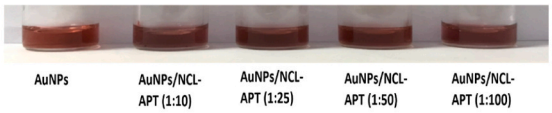

(B)

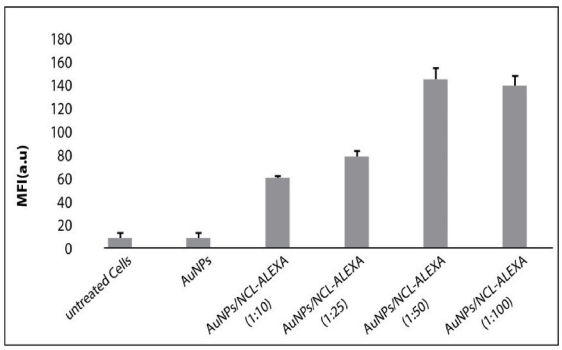

(C)

Fig. 2. Assesment of the colloidal stability and cellular uptake of AuNP/NCL-APT conjugates. (A) Absorption spectra and absorption peak and **(B)** The visual observation of AuNPs conjugated to different concentrations of NCL-APT, and **(C)** Mean Fluorescent Intensity (MFI) for Alexa-Flour 647 obtained from flow cytometry analysis after treatment of MCF-7 cells with AuNP (30 nM) conjugated to Alexa-NCL-APT at different concentrations (10, 25, 50, 100 nM). The values represent mean ± SD of 3 independent experiments.

Table 2
The Characterization of AuNP (30 nM) conjugated to NCL-APT at different concentrations (10, 25, 50, 100 nM). Values represent the mean ± SD of 3 independent experiment.

Formulation	Particle size (d.nm)	Polydispersity index (PDI)	Zeta potential (mV)	Maximum wavelength of the plasmon peak (nm)
AuNP (30 nM) control	28.3+/-6.6	0.37+/-0.01	−27.2+/-2.8	517
AuNP/NCL-APT (1:10) nM	43.6+/-9.3	0.44+/-0.06	−36.7+/-3.1	519
AuNP/NCL-APT (1:25) nM	40.2+/-11.9	0.35+/-0.03	−33.2+/-8.1	519
AuNP/NCL-APT (1:50) nM	47.1+/-5.9	0.36+/-0.02	−40.2+/-1.7	520
AuNP/NCL-APT (1:100) nM	36.6+/-9.1	0.45+/-0.16	−30.1+/-2.1	520

spherical nanoparticles with no significant increase in size. Additionally, Cit-AuNPs displayed an absorption peak at 517 nm (Fig. 1C), which agrees with the measured size by TEM [53], and upon aptamer conjugation, this absorption peak was shifted to 520 nm with no significant broadening or appearance of secondary peaks confirming the colloidal stability of AuNPs during the conjugation reaction (Fig. 1C). Moreover, no visual aggregation or color change was observed upon conjugation, as shown in Fig. 1D. DLS measurements of the prepared AuNP/NCL-APT are reported in Table 1 and indicate an increase in the hydrodynamic diameter of AuNP from 20.9 nm to 55.4 nm, confirming the conjugation of thiolated aptamers. This is further confirmed by the increase in zeta potential of AuNPs upon conjugation from −26.8 ± 4.2 mV to −40.2 ± 1.5 mV, considering that aptamers are strong anionic polyelectrolytes. All of these observations confirmed the successful conjugation of AS1411 aptamer at the surface of AuNP. Our findings are in good agreement with previous studies by Lopes-Nunes et al., 2021 [60], Zhang*et al.*, 2020 [35]; and Ron and Rubinstein, 1998 [61] which suggested that gold nanoparticle can be functionalized with thiolated aptamers through Au–S bonds. Indeed, thiols directly react with the gold surface

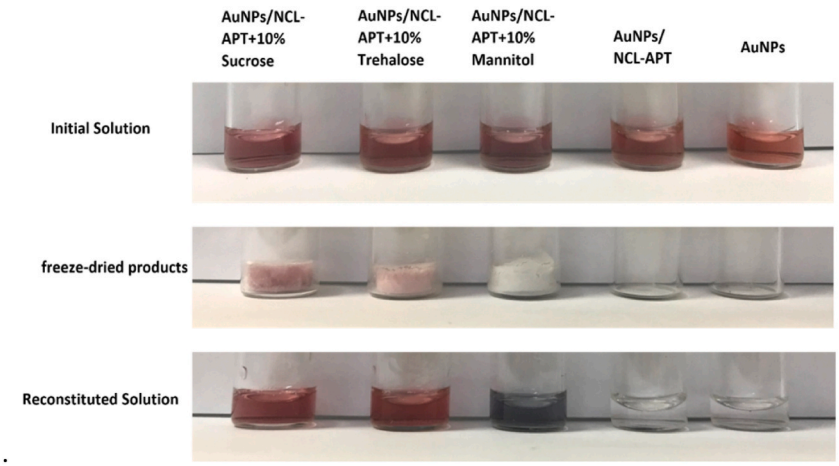

(A)

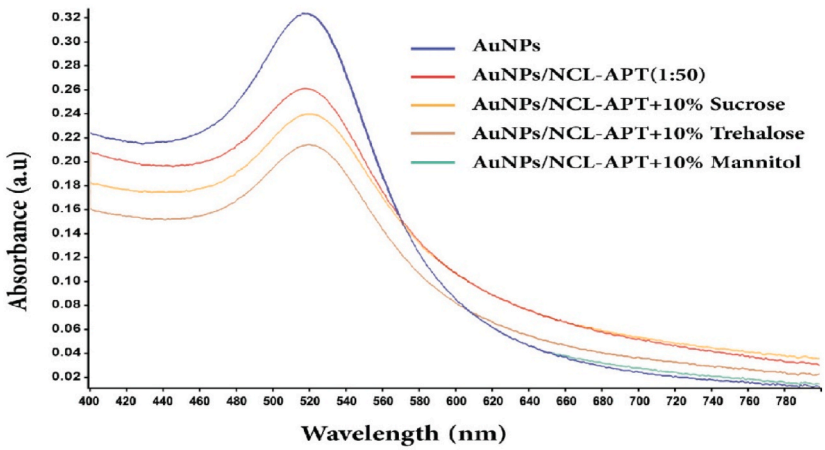

(B)

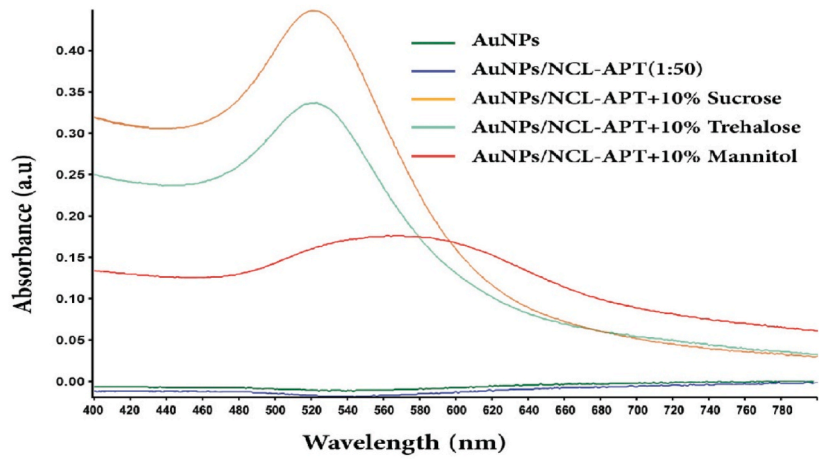

(C)

Fig. 3. **(A)** Photographs of AuNP and AuNP/NCL-APT before lyophilization (upper panel), after lyophilization (middle panel), and after reconstitution with water (bottom panel). Lyophilization was carried out in the absence or presence of different cryoprotectants as labeled. **(B)** Absorption spectra and absorption peak of AuNP and AuNP/NCL-APT before lyophilization in the absence and presence of different cryoprotectants, and **(C)** after Lyophilization and reconstitution with water.

Table 3
The Characterization of AuNPupon lyophilization in the presence of different cryoprotectants. Values represent the mean ± SD of 3 independent experiments.

Formulation	Particle size (d. nm)	Polydispersity index (PDI)	Zeta potential (mV)	Maximum wavelength of the plasmon peak (nm)
AuNPcontrol	30.7+/-9.7	0.41+/-0.05	−29.3+/-3.1	516
AuNP/NCL-APT	52.5+/-10.5	0.46+/-0.06	−38.5+/-7.7	519
AuNP/NCL-APT + 10 % Sucrose	67.4+/-5.4	0.43+/-0.08	−26.1+/-4.4	519
AuNP/NCL-APT + 10 % Trehalose	57.8+/-2.4	0.46+/-0.06	−21.1+/-2.1	521
AuNP/NCL-APT + 10 % Mannitol	90.4+/-4.1	0.42+/-0.12	−29.9+/-2.2	520

to form strong binding energy Au–S bonds, which are widely used in the conjugation of therapeutics, dyes, and nucleic acids to AuNPs [62–64].

To determine the number of NCL-APTs conjugated to each AuNP, a fluorescent ssDNA-binding dye method was used as described in methods. A standard curve was first generated using the recommended standards (400, 200, 100, 50, 25, 12.5, 6.25 ng/well) (Fig. 1E). We found that NCL-APT concentration in AuNP/NCL-APT sample was 12.5 ng/mL, indicating there are approximately 3 NCL-APTs per AuNP. This number represents the possible number of hybridization sites for the aptamer and is consistent with literature values for oligonucleotide coating on various sizes of AuNPs. Furthermore, the measured size of the functionalized conjugates is within the expected size contribution of the added oligonucleotides [57].

To determine the maximum capacity of NCL-APTs that can be attached to a single AuNP, we combined a consistent concentration of AuNP (30 nM) with varying concentrations of NCL-APT (10, 25, 50, 100 nM). Subsequently, we evaluated both the colloidal stability and cellular uptake of the resulting conjugates. The colloidal stability assessment indicated excellent stability in the range of 10–100 nM, demonstrated by the absence of significant broadening or secondary plasmonic peaks in UV–vis spectra (Fig. 2A) and maintained red color (Fig. 2B), suggesting no aggregation. Hydrodynamic diameter measurements by DLS (Table 2) confirmed this, showing a slight increase from 28 nm for citrate-capped AuNP to about 37–47 nm for NCL-APT. Negative surface charges of all NCL-APT at neutral pH were consistent with expectations (Table 2). Overall, mixing AuNP with NCL-APT up to a 3:10 M ratio resulted in a stable colloid suspension without signs of aggregation, suitable for subsequent purification, characterization, and cellular uptake evaluation.

The cellular uptake of AuNP significantly increased upon conjugation with Alexa-NCL-APT, as shown in Fig. 2C, with at least a six-fold increase observed for the lowest NCL-APT concentration. This observation aligns with similar findings that reported enhanced cellular uptake of AuNP upon binding to the AS1411 G-quadruplex [42]. Notably, the observed increase reached plateau for AuNP/Alexa-NCL-APT prepared at a 1:50 M ratio, indicating a maximum saturation of Alexa-NCL-APT on the AuNP surface. Cellular uptake for AuNP prepared by mixing with Alexa-NCL-APT at either a 1:50 or 1:100 M ratios was statistically equivalent, as depicted in Fig. 2C. Based on these results, a 1:50 M ratio was deemed optimal for maximum aptamer density on AuNP, guiding our choice for all subsequent conjugation reactions. Consequently, we focused on evaluating AuNP/NCL-APT prepared at a 1:50 M ratio for further investigations concerning lyophilization and the impact of various cryoprotectants.

3.2. Freeze-drying (lyophilization)

The major goal of this work was to optimize a lyophilization protocol for the prepared AuNP/NCL-APT. Specifically, we aimed to evaluate the colloidal stability and biological activity of AuNP/NCL-APT upon lyophilization in the absence or presence of commonly used cryoprotectants such as mannitol, sucrose, and trehalose. A cryoprotectant concentration of 10 % w/v was considered and used to compare the protective action of all evaluated cryoprotectants, as this concentration is commonly used in lyophilization of therapeutics and nanoparticles [46]. The results showed no color change and no noticeable aggregation upon adding all evaluated cryoprotectants to the AuNP/NCL-APT suspensions, ensuring excellent physical compatibility with AuNP, as shown in Fig. 3A (upper panel) and Fig. 3B. Upon lyophilization, AuNP in vials without cryoprotectants aggregated into very small dried pellets, visually observed and depicted in the empty vials in Fig. 3A (middle panel). However, vials with cryoprotectants exhibited solid lyophilizate with a white-creamy color in the case of mannitol and a reddish color in the cases of sucrose and trehalose (Fig. 3A, middle panel). Upon reconstituting these lyophilizates, a blue suspension indicating nanoparticle aggregation was observed in the case of mannitol (Fig. 3A, lower panel). This observation is substantiated by the pronounced broadening seen in the UV–Vis spectrum of the resulting suspension, depicted in Fig. 3C. In the cases of sucrose and trehalose, reddish suspensions were observed (Fig. 3A, lower panel), accompanied by UV–Vis spectra without significant broadening, as illustrated in Fig. 3C. The observed aggregation or maintained colloidal stability of AuNP/NCL-APT in the absence or presence of various cryoprotectants was further confirmed using DLS measurements, as illustrated in Table 3. The hydrodynamic diameter marginally increased (from 52.5 nm to 57.8 or 67.4 nm) in the presence of sucrose or trehalose, respectively, while it significantly increased (from 52.5 nm to 90.4 nm) in the case of mannitol. Collectively, our results indicate severe aggregation of AuNP in the absence of cryoprotectants. Interestingly, functionalization of AuNP with AuNP/NCL did not alleviate the issue, as we observed similar aggregation and resistance to suspension for AuNP/NCL-APT as well. However, the addition of 10 % mannitol was not sufficient to prevent the observed aggregation completely, and indeed, the resulting lyophilized-reconstituted AuNP/NCL-APT showed significant aggregation. The presence of sucrose or trehalose provided the best protection against aggregation upon lyophilization. Our results are in good agreement with our previouse work where it was found that cryoprotectants were essential in preventing aggregation of citrate-capped or monoclonal antibodies-functionalized AuNP, with

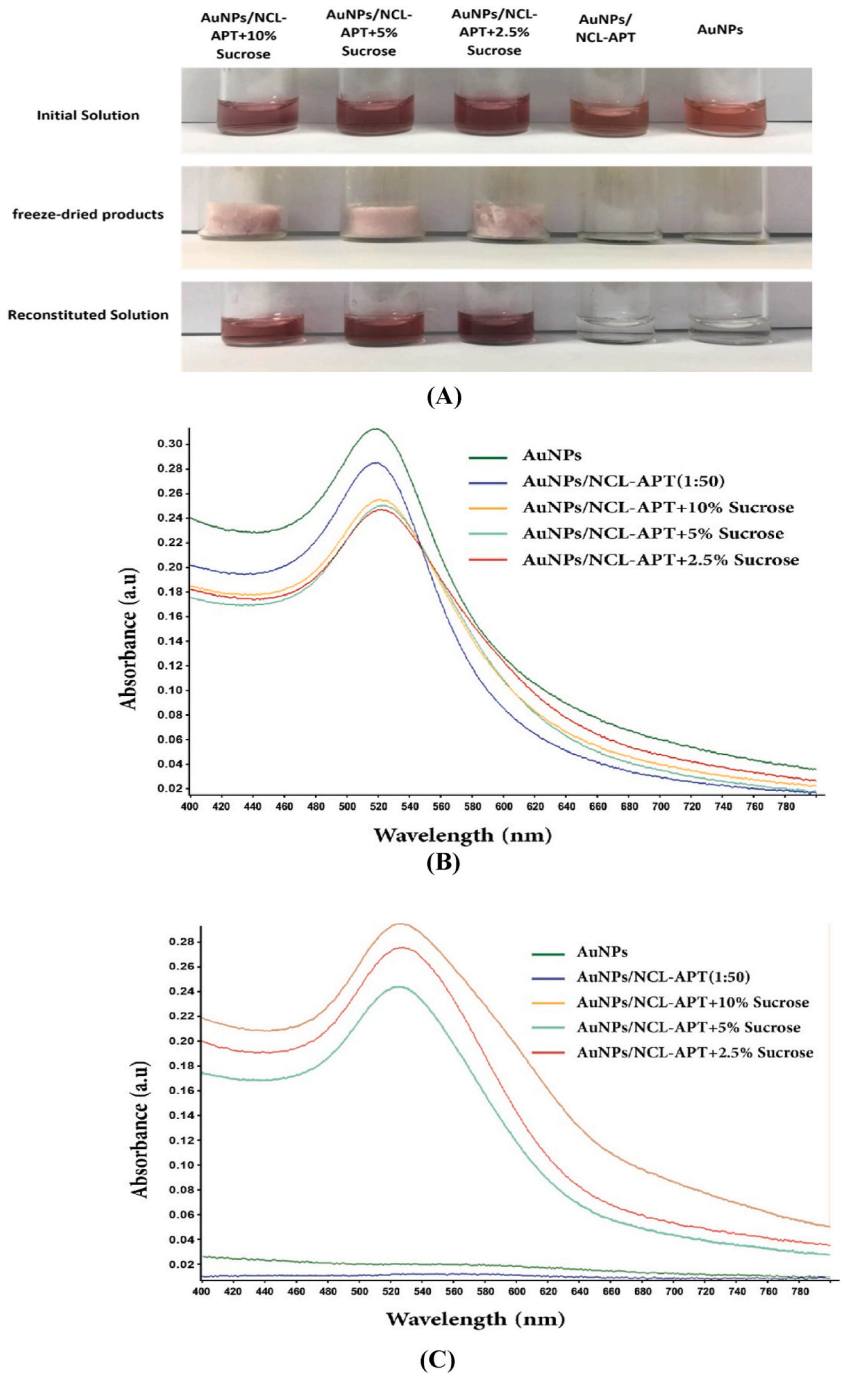

Fig. 4. (A) Photographs of AuNP and AuNP/NCL-APT before lyophilization (upper panel), after lyophilization (middle panel), and after reconstitution with water (bottom panel). Lyophilization was carried out in the absence or presence of different concentrations of Sucrose. **(B and C)** Absorption spectra and absorption peak of AuNP and AuNP/NCL-APT in the absence and presence of different precents of Sucrose before lyophilization and fter lyophilization and reconstitution with water, respectively.

mannitol to offer less protection compared to either sucrose or trehalose [46,47].

Mannitol typically crystallizes in frozen aqueous solutions, displaying a eutectic crystallization exotherm at −22.8 °C. This behavior may contribute to its weak cryoprotective effect, as the formed crystals impose mechanical stress on AuNP surfaces [46]. Studies suggest that the cryoprotective effect of various agents is linked to their ability to form hydrogen bonds with nanoparticles [65]. Mannitol, forming intramolecular hydrogen bonds, exhibits a lower tendency to form hydrogen bonds with citrate-capped AuNP or AuNP/NCL-APT, resulting in a diminished protective effect. The intramolecular hydrogen bonds that mannitol forms, at the expense

Table 4
The Characterization of AuNP and AuNP/NCL-APT before lyophilization in the presence of different levels of sucrose. Values represent the mean ± SD of 3 independent experiments.

Formulation	Particle size (d. nm)	Polydispersity index (PDI)	Zeta potential (mV)	Maximum wavelength of the plasmon peak (nm)
AuNP (30 nM) control	26.4+/-5.1	0.59+/-0.06	−28.6+/-0.74	517
AuNP/NCL-APT (50:1)	59.1+/-6.1	0.46+/-0.07	−36.8+/-2.4	520
AuNP/NCL-APT + 10 % Sucrose	63.8+/-2.8	0.43+/-0.16	−23.1+/-0.61	520
AuNP/NCL-APT + 5 % Sucrose	73.7+/-4.5	0.56+/-0.21	−25.7+/-7.1	522
AuNP/NCL-APT + 2.5 % Sucrose	83.1+/-8.9	0.51+/-0.07	−20.7+/-1.7	521

Table 5
The Characterization of AuNP/NCL-APT after lyophilization in the presence of different precents of Sucrose. Values represent the mean ± SD of 3 independent experiments.

Formulation	Particle size (d. nm)	Polydispersity index (PDI)	Zeta potential (mV)	Maximum wavelength of the plasmon peak (nm)
AuNP/NCL-APT + 10 % Sucrose	71.4+/-6.8	0.37+/-0.23	−26.6+/-3.2	521
AuNP/NCL-APT + 5 % Sucrose	75.2+/-5.5	0.21+/-0.03	−32.7+/-3.2	523
AuNP/NCL-APT + 2.5 % Sucrose	87.3+/-1.8	0.48+/-0.03	−30.7+/-4.9	528

of solute-water hydrogen bonds, explain its lower aqueous solubility compared to sucrose or trehalose [66].

Our findings demonstrate that both sucrose and trehalose effectively prevent aggregation during the lyophilization of AuNP/NCL-APT. Considering the widespread availability and cost-effectiveness of sucrose in typical laboratories compared to trehalose, we proceeded to optimize the amount of sucrose in our formulation. The aim was to identify the minimum quantity necessary to prevent aggregation during the lyophilization process. The results showed that all sucrose levels (2.5–10 % w/w) formed a pale red cake structure after lyophilization (Fig. 4A, middle panel) and red suspension upon reconstitution with water (Fig. 4A, bottom panel), confirming the protective action of sucrose at all evaluated concentrations (Fig. 4A). UVvis spectrum before and after lyophiliztion (Fig. 4B and C, respectively) supports this observed protective effect as no sever broadening is observed even at the lowest sucrose level. Furthermore, The observed protective effects or maintained colloidal stability of sucrose against the aggregation of AuNP/NCL-APT upon lyophilization was further confirmed using DLS measurements, as illustrated in Table 4 and Table 5.

3.3. Cellular and functional analyses of AuNP/NCL-APT before and after lyophilization with 10 % sucrose

Subsequent to investigating the colloidal stability of AuNP/NCL-APT after lyophilization and optimizing the type and level of cryoprotectants, our objective was to assess the selective cellular uptake of AuNP/NCL-APT, both pre- and post-lyophilization. We employed the MCF-7 cell line, chosen for its established overexpression of NCL receptors [67]. The cellular uptake was investigated by flow cytometry analysis after 24 h of treatment, which reflected the recovery of the fluorescent signal obtained from Alexa fluor 647-labeled aptamer internalization into the cells. Untreated cells and cells treated with free AuNPs served as negative control, while free Alexa fluor 647 served as positive control. The results revealed a successful uptake of AuNP/NCL-APT conjugates by MCF-7 cells as compared to untreated cells or cells treated with free AuNP ($P < 0.05$), and that there was no significant difference in internalization between lyophilized and non-lyophilized conjugates ($P = 0.33$) (Fig. 5A). This indicates retaining the colloidal stability of AuNP/NCL-APT upon lyophilization in the presence of sucrose. These results are consistent with a previous study by Malik et al., 2015 [16] in which AS1411- linked gold nanospheres had a superior cellular uptake and showed selectivity for cancer cells compared to non-malignant cells in a mouse model of breast cancer.

Specific uptake of NCL-APT by MCF-7 cells and its accumulation in the perinuclear region of the cytoplasm has been documented [68], thus, CLSM was performed to evaluate the cellular uptake, accumulation, and localization of lyophilized and non-lyophilized AuNP/NCL-APT conjugates. Confocal microscopy images demonstrated a specific accumulation of free NCL-APT and AuNP/NCL-APT conjugates around the nuclei of MCF-7 cells compared to free AuNP (Fig. 5B), which confirmed our flow cytometry results (Fig. 5A) and illustrated a successful targeting and an enhanced tumor affinity of AuNP upon conjugation to NCL-APT. This is consistent with a previous study by Zhu et al., 2017 [69], in which AuNP/NCL-APT exhibited an improved biostability, and the synergy of multivalent NCL-APT–nucleolin binding promoted accumulation of the nanocomposite towards cancer cells and subsequent internalization, resulting in a highly specific cancer cell-targeting under low AuNP/NCL-APT concentration range.

To evaluate the biological effect of AuNP/NCL-APT before and after lyophilization, qRT-PCR was performed to determine *Bcl-2* gene expression; a gene which mRNA life span is known to increase by its interaction with nucleolin [70]. Subsequntly, successful targeting of nucleolin by AuNP/NCL-APT should result in reduced gene expression of *Bcl-2*. As shown in Fig. 5C, cell treatment with free AuNP and free NCL-APT stimulated a non significant ~2 folds and 1 fold decrease in *Bcl-2* expression, respectively, compared to untreated cells. Consistently, a previous study showed that free AuNP at up to 200 μg/mL exerted a concentration-dependent cytotoxicity and a significant downregulation of *Bcl-2* in MCF-7 cells [71].

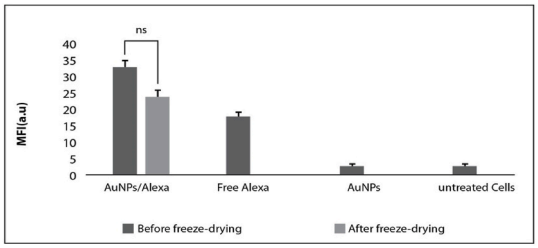

(A)

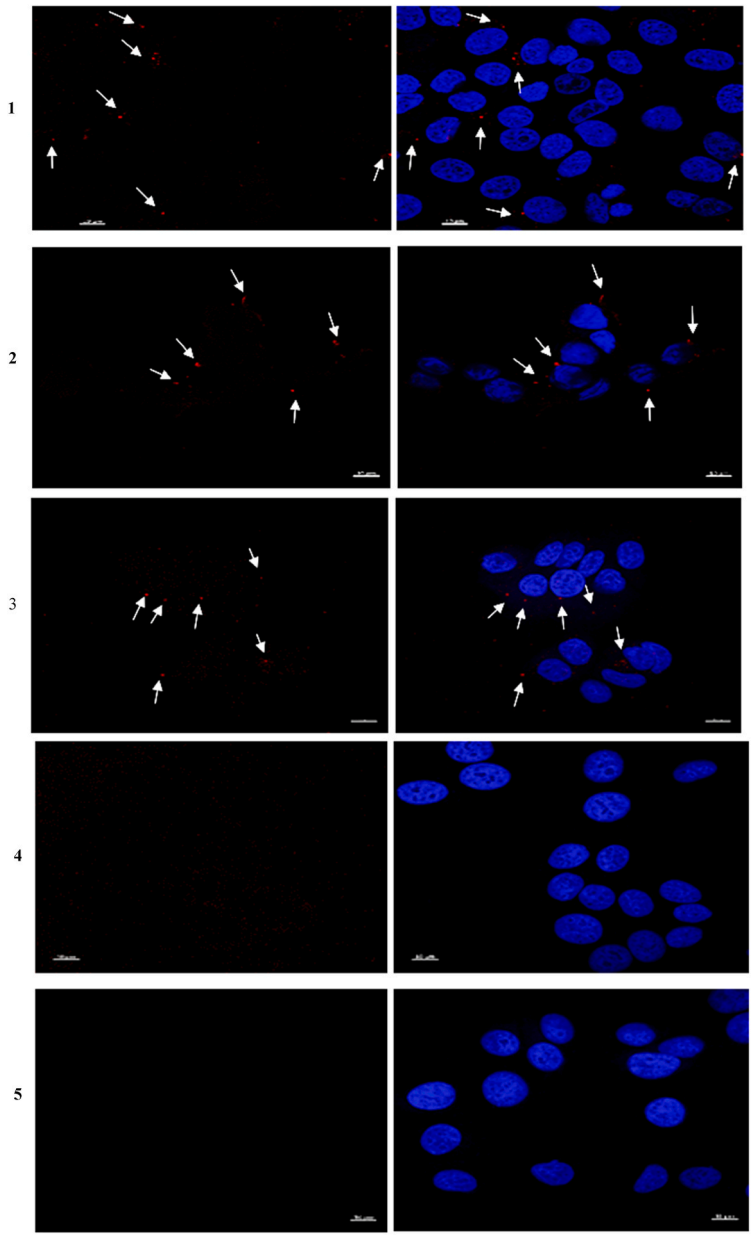

(B)

Fig. 5. Cellular and functional analysis of AuNP/NCL-APT upon lyophilization. (A) Mean Fluorescent Intensity (MFI) of Alexa-Flour 647 for AuNP/NCL-APT before and after lyophilization with 10 % sucrose obtained from flow cytometry analysis of treated MCF-7 cells. Values represent mean ± SD of 3 independent experiments ($P > 0.05$). **(B)** Confocal images of MCF-7 cells. Cell nuclei are depicted in blue and AS1411 is depicted in red. **1)** Cells treated with non-lyophilized AuNP/NCL -APT, **2)** Cells treated with lyophilized AuNP/NLC -APT, **3)** Cells treated with free NCL-APT.**4)**

Cells treated with free AuNP, and **5)** Untreated cells. **(C)** Q-RT-PCR analysis of Bcl-2 expression in MCF-7 cells treated with non-lyophilized or lyophilized AuNP/NCL-APT, free NCL-APT, and free AuNP, as compared to untreated cells. Data represent Mean ± SD of 3 independent experiments, $P < 0.05$. (For interpretation of the references to color in this figure legend, the reader is referred to the Web version of this article.)

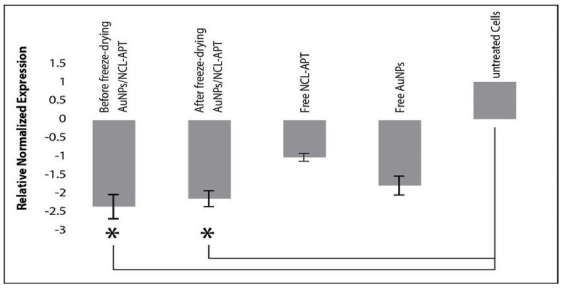

(C)

Fig. 5. (*continued*).

On the other hand, both non-lyophilized and lyophilized AuNP/NCL-APT equally induced a 2-fold decrease in *Bcl-2* gene expression, as compared to untreated control cells and free NCL-APT ($P < 0.05$) (Fig. 5C). These results support the findings by Soundararajan et al., 2008 [68], which suggested that NCL-APT performs as a molecular decoy by competing with *Bcl*-2 mRNA for binding to cytoplasmic nucleolin in breast cancer cells, causing destabilization of *Bcl*-2 mRNA [72]. Additionally, our results indicate that conjugation of NCL-APT to AuNP enhanced aptamer targeting of nucleolin.

4. Conclusion

In the current study, AuNP were successfully synthesized with size and plasmon properties that can be described as suitable candidates for biomedical applications. Moreover, an optimized bioconjugation protocol of NCL-APT to AuNP was developed. The created conjugates may serve as a clinically relevant model for bio-conjugated nanoparticles for different biomedical applications, and the model was systemically evaluated for colloidal stability and biological activity upon lyophilization in the absence and presence of trehalos, manitose, and sucrose cryoprotectants. Consequently, AuNP/NCL-APT demonstrated irreversible aggregation in the absence of cryoprotectants, but 10 % (w/w) sucrose proved to be the best excipient to maintain AuNP colloidal stability. AuNP nano delivery to MCF-7 cells was enhanced by NCL-APT, as confirmed via flow cytometry, CLSM analysis, and Q-RT-PCR analysis of *Bcl-2* gene expression assay. Ultimately, this study is essential for future preclinical examinations and opens new insights into cancer treatment and diagnosis regimens.

Ethics declaration

Review and/or approval by an ethics committee was not needed for this study because it does not involve experiments on humans or animals.

Informed consent was not required for this study because it does not involve experiments on humans.

Funding

This study was funded by the thesis-oriented fund granted by the deanship of research at Jordan University of science and technology (grant # 2020/0493).

Data availability

No data was used for the research described in the article.

CRediT authorship contribution statement

Dalya Saidi: Writing – original draft, Investigation, Data curation. **Marya Obeidat:** Writing – review & editing, Supervision, Funding acquisition. **Shrouq Alsotari:** Data curation. **Abed-Alqader Ibrahim:** Data curation. **Rula Al-Buqain:** Data curation. **Suha Wehaibi:** Data curation. **Dana A. Alqudah:** Data curation. **Hamdi Nsairat:** Data curation. **Walhan Alshaer:** Writing – review & editing, Validation, Project administration, Methodology, Investigation, Conceptualization. **Alaaldin M. Alkilany:** Writing – review & editing, Validation, Supervision.

Declaration of competing interest

The authors declare that they have no known competing financial interests or personal relationships that could have appeared to influence the work reported in this paper.

References

[1] J. Blair, Making magic bullets, Nat Microbiol 2 (2017) 17110.
[2] O.C. Farokhzad, R. Langer, Impact of nanotechnology on drug delivery, ACS Nano 3 (1) (2009) 16–20.
[3] W. Alshaer, H. Hillaireau, E. Fattal, Aptamer-guided nanomedicines for anticancer drug delivery, Adv. Drug Deliv. Rev. 134 (2018) 122–137.
[4] M.J. Mitchell, et al., Engineering precision nanoparticles for drug delivery, Nat. Rev. Drug Discov. 20 (2) (2021) 101–124.
[5] A.M. Alkilany, et al., Ligand density on nanoparticles: a parameter with critical impact on nanomedicine, Adv. Drug Deliv. Rev. 143 (2019) 22–36.
[6] A. Heuer-Jungemann, et al., The role of ligands in the chemical synthesis and applications of inorganic nanoparticles, Chem. Rev. 119 (8) (2019) 4819–4880.
[7] S.D. Jayasena, Aptamers: an emerging class of molecules that rival antibodies in diagnostics, Clin. Chem. 45 (9) (1999) 1628–1650.
[8] A.D. Ellington, J.W. Szostak, In vitro selection of RNA molecules that bind specific ligands, Nature 346 (6287) (1990) 818–822.
[9] C. Tuerk, L. Gold, Systematic evolution of ligands by exponential enrichment: RNA ligands to bacteriophage T4 DNA polymerase, science 249 (4968) (1990) 505–510.
[10] Y. Zhang, B.S. Lai, M. Juhas, Recent advances in aptamer discovery and applications, Molecules 24 (5) (2019) 941.
[11] E.M. Reyes-Reyes, et al., Mechanistic studies of anticancer aptamer AS1411 reveal a novel role for nucleolin in regulating Rac 1 activation, Mol. Oncol. 9 (7) (2015) 1392–1405.
[12] S.I. Ismail, W. Alshaer, Therapeutic aptamers in discovery, preclinical and clinical stages, Adv. Drug Deliv. Rev. 134 (2018) 51–64.
[13] P.S. Kozani, P.S. Kozani, M.T. Malik, AS1411-functionalized delivery nanosystems for targeted cancer therapy, Explor Med 2 (2021) 146–166.
[14] M. Keshtkar, et al., Aptamer-conjugated magnetic nanoparticles as targeted magnetic resonance imaging contrast agent for breast cancer, J Med Signals Sens 6 (4) (2016) 243–247.
[15] X. Tong, et al., Progress in cancer drug delivery based on AS1411 oriented nanomaterials, J. Nanobiotechnol. 20 (1) (2022) 57.
[16] M.T. Malik, et al., AS1411-conjugated gold nanospheres and their potential for breast cancer therapy, Oncotarget 6 (26) (2015) 22270–22281.
[17] S.S. Mehrnia, et al., Radiosensitization of breast cancer cells using AS1411 aptamer-conjugated gold nanoparticles, Radiat. Oncol. 16 (1) (2021) 33.
[18] X. Tong, et al., Progress in cancer drug delivery based on AS1411 oriented nanomaterials, J. Nanobiotechnol. 20 (1) (2022) 57.
[19] H. Motaghi, M.A. Mehrgardi, P. Bouvet, Carbon dots-as1411 aptamer nanoconjugate for ultrasensitive spectrofluorometric detection of cancer cells, Sci. Rep. 7 (1) (2017) 10513.
[20] J.E. Rosenberg, et al., A phase II trial of AS1411 (a novel nucleolin-targeted DNA aptamer) in metastatic renal cell carcinoma, Invest. N. Drugs 32 (1) (2014) 178–187.
[21] A.M. Alkilany, et al., PLGA-gold nanocomposite: preparation and biomedical applications, Pharmaceutics 14 (3) (2022) 660.
[22] A.M. Alkilany, S.E. Lohse, C.J. Murphy, The gold standard: gold nanoparticle libraries to understand the nano-bio interface, Accounts Chem. Res. 46 (3) (2013) 650–661.
[23] A. Yañez-Aulestia, et al., Gold nanoparticles: current and upcoming biomedical applications in sensing, drug, and gene delivery, Chem. Commun. 58 (78) (2022) 10886–10895.
[24] M. Nejabat, et al., An overview on gold nanorods as versatile nanoparticles in cancer therapy, J. Contr. Release 354 (2023) 221–242.
[25] Z. Akter, F.Z. Khan, M. Khan, Gold nanoparticles in triple-negative breast cancer therapeutics, Curr. Med. Chem. 30 (3) (2023) 316–334.
[26] A. Jahangiri-Manesh, et al., Gold nanorods for drug and gene Delivery: an overview of recent advancements, Pharmaceutics 14 (3) (2022) 664.
[27] Y. Wu, M.R. Ali, K. Chen, N. Fang, M.A. El-Sayed, Gold nanoparticles in biological optical imaging, Nano Today 24 (2019 Feb 1) 120–140.
[28] Y. Ran, T. Wang, Y. He, F. Zhao, B. Zeng, Fabrication of electrochemiluminescence aptasensor for PD-L1 detection based on luminescent CdS@ Ce-MOF@ Au, Microchem. J. 22 (2023 Jun) 109005.
[29] J. Milan, K. Niemczyk, M. Kus-Liśkiewicz, Treasure on the earth-gold nanoparticles and their biomedical applications, Materials 15 (9) (2022).
[30] I. Hammami, et al., Gold nanoparticles: synthesis properties and applications, J. King Saud Univ. Sci. 33 (7) (2021) 101560.
[31] Y.-C. Yeh, B. Creran, V.M. Rotello, Gold nanoparticles: preparation, properties, and applications in bionanotechnology, Nanoscale 4 (6) (2012) 1871–1880.
[32] Y.-C. Yeh, B. Creran, V. Rotello, Gold nanoparticles: preparation, properties, and applications in bionanotechnology, Nanoscale 4 (2011) 1871–1880.
[33] P. Bayat, et al., Aptamer AS1411-functionalized gold nanoparticle-melittin complex for targeting MCF-7 breast cancer cell line, Nanomedicine Journal 9 (2) (2022) 164–169.
[34] S.S. Mehrnia, et al., Radiosensitization of breast cancer cells using AS1411 aptamer-conjugated gold nanoparticles, Radiat. Oncol. 16 (1) (2021).
[35] Y. Zhang, et al., Synthesis and application of AS1411-functionalized gold nanoparticles for targeted therapy of gastric cancer, ACS Omega 5 (48) (2020) 31227–31233.
[36] A. Kardani, et al., Inhibition of miR-155 in MCF-7 breast cancer cell line by gold nanoparticles functionalized with antagomir and AS1411 aptamer, J. Cell. Physiol. 235 (10) (2020) 6887–6895.
[37] M. Baneshi, et al., A novel theranostic system of AS1411 aptamer-functionalized albumin nanoparticles loaded on iron oxide and gold nanoparticles for doxorubicin delivery, Int. J. Pharm. 564 (2019) 145–152.
[38] S. Kabirian-Dehkordi, et al., AS1411-conjugated gold nanoparticles affect cell proliferation through a mechanism that seems independent of nucleolin, Nanomed. Nanotechnol. Biol. Med. 21 (2019).
[39] F. Ghahremani, et al., AS1411 aptamer-targeted gold nanoclusters effect on the enhancement of radiation therapy efficacy in breast tumor-bearing mice, Nanomedicine 13 (20) (2018) 2563–2578.
[40] F. Ghahremani, et al., AS1411 aptamer conjugated gold nanoclusters as a targeted radiosensitizer for megavoltage radiation therapy of 4T1 breast cancer cells, RSC Adv. 8 (8) (2018) 4249–4258.
[41] M.T. Malik, et al., AS1411-conjugated gold nanospheres and their potential for breast cancer therapy, Oncotarget 6 (26) (2015) 22270–22281.
[42] J. Ai, et al., Multifunctional AS1411-functionalized fluorescent gold nanoparticles for targeted cancer cell imaging and efficient photodynamic therapy, Talanta 118 (2014) 54–60.
[43] W. Zhao, et al., DNA aptamer folding on gold nanoparticles: from colloid chemistry to biosensors, J. Am. Chem. Soc. 130 (11) (2008) 3610–3618.
[44] V.A. Miron-Merida, et al., Aptamer-target-gold nanoparticle conjugates for the quantification of fumonisin B1, Biosensors 11 (1) (2021).
[45] K.A. Kang, M.D. Nguyen, Gold nanoparticle-based fluorescent contrast agent with enhanced sensitivity, Adv. Exp. Med. Biol. 977 (2017) 399–407.
[46] A.M. Alkilany, et al., Colloidal stability of citrate and mercaptoacetic acid capped gold nanoparticles upon lyophilization: effect of capping ligand attachment and type of cryoprotectants, Langmuir 30 (46) (2014) 13799–13808.
[47] M.A. Hamaly, et al., Freeze-drying of monoclonal antibody-conjugated gold nanorods: colloidal stability and biological activity, Int. J. Pharm. 550 (1–2) (2018) 269–277.
[48] G. Degobert, D. Aydin, Lyophilization of nanocapsules: instability sources, formulation and process parameters, Pharmaceutics 13 (8) (2021).
[49] R. Kumar, B.N. Kharbikar, Lyophilized yeast powder for adjuvant free thermostable vaccine delivery, Appl. Microbiol. Biotechnol. 105 (8) (2021) 3131–3143.
[50] N.G. Bastús, J. Comenge, V. Puntes, Kinetically controlled seeded growth synthesis of citrate-stabilized gold nanoparticles of up to 200 nm: size focusing versus ostwald ripening, Langmuir 27 (17) (2011) 11098–11105.

[51] F. Caputo, et al., Measuring particle size distribution by asymmetric flow field flow fractionation: a powerful method for the preclinical characterization of lipid-based nanoparticles, Mol. Pharm. 16 (2) (2019) 756–767.
[52] F. Odeh, et al., Remote loading of curcumin-in-modified β-cyclodextrins into liposomes using a transmembrane pH gradient, RSC Adv. 9 (64) (2019) 37148–37161.
[53] W. Haiss, N.T. Thanh, J. Aveyard, D.G. Fernig, Determination of size and concentration of gold nanoparticles from UV− Vis spectra, Anal. Chem. 79 (11) (2007 Jun 1) 4215–4221.
[54] W. Alshaer, H. Hillaireau, J. Vergnaud, S. Mura, C. Deloménie, F. Sauvage, S. Ismail, E. Fattal, Aptamer-guided siRNA-loaded nanomedicines for systemic gene silencing in CD-44 expressing murine triple-negative breast cancer model, J. Contr. Release 271 (2018 Feb 10) 98–106.
[55] H. Xu, et al., Aptamer-functionalized gold nanoparticles as probes in a dry-reagent strip biosensor for protein analysis, Anal. Chem. 81 (2) (2009) 669–675.
[56] X. Ni, et al., Nucleic acid aptamers: clinical applications and promising new horizons, Curr. Med. Chem. 18 (27) (2011) 4206–4214.
[57] D.J. Javier, et al., Aptamer-targeted gold nanoparticles as molecular-specific contrast agents for reflectance imaging, Bioconjugate Chem. 19 (6) (2008) 1309–1312.
[58] H. Nsairat, et al., Grafting of anti-nucleolin aptamer into preformed and remotely loaded liposomes through aptamer-cholesterol post-insertion, RSC Adv. 10 (59) (2020) 36219–36229.
[59] C.A. Fassbinder-Orth, Methods for quantifying gene expression in ecoimmunology: from qPCR to RNA-Seq, Integr. Comp. Biol. 54 (3) (2014) 396–406.
[60] J. Lopes-Nunes, et al., Aptamer-functionalized gold nanoparticles for drug delivery to gynecological carcinoma cells, Cancers 13 (16) (2021).
[61] H. Ron, I. Rubinstein, Self-assembled monolayers on oxidized metals. 3. Alkylthiol and dialkyl disulfide assembly on gold under electrochemical conditions, J. Am. Chem. Soc. 120 (51) (1998) 13444–13452.
[62] Y. Xue, et al., Quantifying thiol–gold interactions towards the efficient strength control, Nat. Commun. 5 (1) (2014) 4348.
[63] L.L. Rouhana, M.D. Moussallem, J.B. Schlenoff, Adsorption of short-chain thiols and disulfides onto gold under defined mass transport conditions: coverage, kinetics, and mechanism, J. Am. Chem. Soc. 133 (40) (2011) 16080–16091.
[64] Y. Xue, et al., Quantifying thiol–gold interactions towards the efficient strength control, Nat. Commun. 5 (2014).
[65] D. Quintanar-Guerrero, et al., Influence of the stabilizer coating layer on the purification and freeze-drying of poly(D,L-lactic acid) nanoparticles prepared by an emulsion-diffusion technique, J. Microencapsul. 15 (1) (1998) 107–119.
[66] G. Caron, J. Kihlberg, G. Ermondi, Intramolecular hydrogen bonding: an opportunity for improved design in medicinal chemistry, Med. Res. Rev. 39 (5) (2019) 1707–1729.
[67] J. Wu, et al., Nucleolin targeting AS1411 modified protein nanoparticle for antitumor drugs delivery, Mol. Pharm. 10 (10) (2013) 3555–3563.
[68] S. Soundararajan, et al., The nucleolin targeting aptamer AS1411 destabilizes Bcl-2 messenger RNA in human breast cancer cells, Cancer Res. 68 (7) (2008) 2358–2365.
[69] Y.J. Zhu, W.J. Li, Z.Y. Hong, A.N. Tang, D.M. Kong, Stable, polyvalent aptamer-conjugated near-infrared fluorescent nanocomposite for high-performance cancer cell-targeted imaging and therapy, J. Mater. Chem. B 5 (46) (2017) 9229–9237.
[70] D. Ishimaru, et al., Mechanism of regulation of bcl-2 mRNA by nucleolin and A+U-rich element-binding factor 1 (AUF1), J. Biol. Chem. 285 (35) (2010) 27182–27191.
[71] S. Kabirian-Dehkordi, et al., AS1411-conjugated gold nanoparticles affect cell proliferation through a mechanism that seems independent of nucleolin, Nanomedicine 21 (2019) 102060.
[72] M.E. Selim, A.A. Hendi, Gold nanoparticles induce apoptosis in MCF-7 human breast cancer cells, Asian Pac. J. Cancer Prev. APJCP 13 (4) (2012) 1617–1620.